Nuclear Science and Techniques (2025) 36:197
https://doi.org/10.1007/s41365-025-01774-5

XAFS platform at NFPS BL17B at SSRF: extending structural characterization from long-range to short-range orders

Lan-Lu Lu[1,2,3] · Wen-Ming Qin[2] · Luo-Zhen Jiang[2] · Yang Liu[2] · Kang-Wen Bao[2] · Chun-Yu Li[2] · Zhong-Jie Zhu[2] · Yi-Jun Gu[2] · Jian-Chao Tang[2] · Qing-Jie Xiao[2] · Ting-Ting Wu[2] · Yu-Pu Zhang[2] · Wei-Zhe Zhang[2] · Shu-Yu Zhou[2] · Ya-Yun Yang[4] · Zheng Jiang[5]

Received: 24 July 2024 / Revised: 25 September 2024 / Accepted: 30 September 2024 / Published online: 13 August 2025

Abstract

The synchrotron radiation beamline BL17B of the National Facility for Protein Science (NFPS) in Shanghai, situated at the Shanghai Synchrotron Radiation Facility (SSRF), was originally designed for diffraction experiments and accommodates techniques including single-crystal diffraction, powder diffraction, and grazing-incidence wide-angle X-ray scattering (GIWAXS) to enable the characterization of long-range ordered atomic structures. The academic community associated with BL17B engages in research domains encompassing biology, environment, energy, and materials, and a pronounced demand for characterizing short-range ordered structures exists. To address these requirements, BL17B established an advanced X-ray absorption fine structure (XAFS) experimental platform that enabled it to address a wide range of systems, from crystalline to amorphous and from long-range order to short-range order. The XAFS platform allows simultaneous XAFS data acquisition for both the transmission and fluorescence modes within an energy range of 5–23 keV, encompassing the K-edges of titanium to ruthenium and the L3-edges of cesium to bismuth. The platform exemplifies high levels of automation achieved through automated sample assessment and data collection based on large-capacity sample wheels that facilitate remote sample loading. When integrated with a highly integrated control system that simplifies experimental preparation and data collection, the XAFS platform significantly bolsters experimental efficiency and enhances user experience. Notably, the platform boasts an impressively low extended X-ray absorption fine structure (EXAFS) detection limit of 0.04 wt% for dilute copper phthalocyanine (CuPc) samples and an even more remarkable X-ray absorption near edge structure (XANES) detection threshold of 0.01 wt%. These results demonstrate the methodology's reliability in low-concentration sample analysis, confirming its capability to generate high-quality XAFS data.

Keywords XAFS · Synchrotron radiation · Short-range order

1 Introduction

Beamline BL17B at the Shanghai Synchrotron Radiation Facility (SSRF) [1], which is affiliated with the National Facility for Protein Science in Shanghai (NFPS) (https://nfpss.sari.ac.cn), was originally conceived to conduct

This study was supported by the Chinese Academy of Science (CAS) Key Technology Talent Program (No. 2021000022). We express our appreciation to the National Facility for Protein Science (NFPS) in Shanghai and Shanghai Synchrotron Radiation Facility (SSRF) teams for their tremendous support throughout the project, including design, installation, testing, and ongoing collaboration.

✉ Wen-Ming Qin
qinwenming@sari.ac.cn

[1] Shanghai Institute of Applied Physics, Chinese Academy of Sciences, Shanghai 201800, China

[2] National Facility for Protein Science in Shanghai, Shanghai Advanced Research Institute, Chinese Academy of Sciences, Shanghai 201210, China

[3] University of Chinese Academy of Sciences, Beijing 100049, China

[4] KEENON Robotics Company Limited, Shanghai 201206, China

[5] National Synchrotron Radiation Laboratory, University of Science and Technology of China, Hefei 230029, China

high-throughput protein crystallography [2–4] investigations. Beamline BL17B supports techniques such as single-crystal diffraction [5, 6], powder diffraction [7], and grazing-incidence wide-angle X-ray scattering (GIWAXS) [8–10] to enable the characterization of long-range ordered atomic structures. Beyond its applications in structural biology [11–13], this beamline supports scientific research across diverse domains, including the environment [14, 15], energy [16, 17], and materials [18–20]. In these fields, investigators frequently require an understanding of the structural order at a scale of a few angstroms, namely, the short-range order. Although traditional crystallographic techniques reveal long-range ordered crystal structures, they may not adequately capture the local amorphous nature of such short-range ordered features. For instance, research on transition metal-containing biological systems necessitates local structural insights into metal sites related to functional diversity [21, 22]. In biomedical and ecological environmental research, understanding the local coordination of exogenous metals within bio-macromolecules and their transformation processes are essential in the revelation of their interaction mechanisms [14, 23, 24]. Similarly, studying the catalytic processes and mechanisms of metal–organic frameworks (MOFs), covalent–organic frameworks (COFs), and their derivatives in materials research requires knowledge of the active sites along with the local atomic coordination and chemical state [25, 26]. Research on perovskite solar cells also benefits from short-range ordered structural characterization to assess the impacts of nanoscale phase impurities on the film quality [27].

X-ray absorption fine structure (XAFS) [28, 29] techniques can be used to probe local atomic and electronic environments within ranges of approximately 0.5–5 Å surrounding the element-specific absorbing centers in short-range ordered structures. Moreover, XANES, the near-edge region of XAFS, reveals details regarding oxidation states, electron orbital occupation, and coordination symmetries. In EXAFS, the extended XAFS oscillations provide information on the atomic distances, coordination numbers, and species of neighboring atoms. The XAFS technique effectively compensates for the limitations of crystallography in characterizing short-range order structures and offers the advantage of being adaptable to various sample forms. That is, XAFS is not limited to crystal structures alone. Beamline BL17B possesses the optical foundation and spatial conditions required to develop an XAFS experimental technique. Thus, we constructed a novel XAFS platform at BL17B to extend our structural characterization capabilities from long-to short-range orders. This study provides a valuable reference for similar upgrade projects in synchrotron facilities.

2 Basis for upgrade

The existing optical configuration of BL17B is primarily designed to accommodate the requirements of single-crystal diffraction experiments. A schematic of the main optical components of BL17B is shown in Fig. 1. The SSRF was operated at an electron energy of 3.5 GeV with a current of 220 mA in top-up mode. The X-ray photon source was a bending magnet with a magnetic field of 1.27 T, and it generated a white beam with a critical energy of 10.3 keV. The beam was confined through a 1.5 mrad × 0.1 mrad ($H \times V$)-wide white beam slit, namely, Slit1, which selected the central cone to alleviate the radiation and thermal loads on downstream optics. The beam was subsequently collimated vertically into a quasi-parallel beam to improve the energy resolution. The collimating mirror is set at a grazing-incidence angle of 2.8 mrad and features 2 reflection stripes, namely, a Si coating used below 8 keV and a Rh coating used at 8–23 keV. This system suppressed the harmonic contamination relative to the fundamental to be below 10^{-3}. A fixed-exit Si(111) double-crystal monochromator (DCM) then converted the white beam into a monochromatic beam with an energy resolution of 2×10^{-4} within the 5–23 keV range. Slit2 further refined the beam to decrease its size. Finally, the monochromatic X-rays were focused using a Rh-coated toroidal mirror at a grazing-incidence angle of 2.8 mrad. The focal point, which was 42 m from the source, served as the diffractometer sample position with a beam size of 150 μm × 180 μm ($H \times V$) and divergence of 1.5 mrad × 0.2 mrad ($H \times V$) to provide a flux of 2×10^{11} photons/s at 12 keV.

Considering the feasibility of incorporating XAFS experiments at BL17B, the current monochromatic beam energy range, energy resolution, and flux meet the requirements for the XAFS experiment. However, further suppression of harmonic content is required. For XAFS, the acceptable level of harmonic contamination relative to the fundamental signal is generally below 10^{-4} [30], as harmonics can

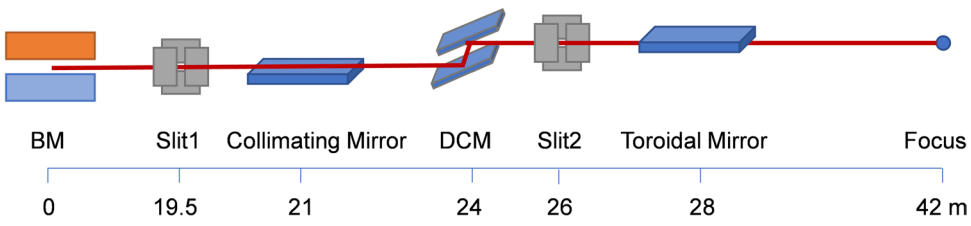

Fig. 1 (Color online) Schematic of the optical configuration at BL17B

lead to amplitude attenuation in the XAFS spectra owing to the effect of undesirable photons [31, 32]. Currently, only energies greater than 10 keV satisfy this criterion. By introducing dedicated harmonic rejection mirrors, the 5–10 keV region can also be rendered compatible. In terms of experimental space, an approximately 2 m segment that is primarily occupied by vacuum pipes exists between the Be window exit and diffractometer in the experimental hutch (highlighted in the red box in the left panel of Fig. 2). This space can accommodate an XAFS station with the XAFS sample positioned approximately 1 m upstream of the diffraction sample. Adjusting the grazing-incidence angle and height of the toroidal mirror focuses the XAFS sample position. By mounting both the XAFS setup and a vacuum tube for the diffraction experiment on a platform that can move perpendicularly to the optical path, rapidly switching between XAFS and diffraction modes becomes convenient. The image on the right in Fig. 2 shows the experimental hutch after incorporating the XAFS station according to the proposed scheme.

3 XAFS experimental station

We added an XAFS experimental station in the beam path upstream of the diffraction experiment station. As depicted in Fig. 3, the XAFS experimental station consisted of two main parts: (1) a standalone harmonic rejection mirror (HRM) installed on the floor and (2) an XAFS testing platform installed on the existing support stage equipped with a slit, XAFS sample holder, detector, and vacuum tube. A slit was used to shape the incident beam and restrict the scattered photons around the central cone. When the vacuum tube was moved in, it switched to the diffraction mode, and the I3 ionization chamber remained in the beam path to monitor the incident beam intensity.

3.1 Harmonic rejection mirror (HRM)

The reflectivity of materials for grazing incidence X-rays is nearly 100% below the critical energy but drops sharply above the critical energy [33]. Therefore, a grazing incidence plane mirror can be considered a low-pass filter for X-rays used to suppress higher-order harmonics. Based on this principle, the HRM employs a pair of pre-aligned and parallel-plane mirror designs, as shown in Fig. 4. The plane mirror had 200 mm long Ni and Rh stripes on the Si substrate, and the grazing angle was fixed at 5.8 mrad. The mirrors were placed in parallel with a 100 mm offset and were separated vertically by 0.58 mm. This design further suppressed harmonics at energies above 5 keV to ensure that the XAFS amplitude attenuation caused by harmonics was less than 1%. The HRM was positioned 40.2 m downstream of the source and could fully receive the main beam. These settings reflected the fundamental flux with efficiencies of 88% and 65% for the Ni and Rh coatings, respectively. The HRM design ensured the suppression of high-order harmonics without excessively affecting the beam size and light flux downstream. The Ni coating worked from 5–8 keV, whereas the Rh coating worked from 5.5–11 keV. In the overlapping zone (5.5–8 keV), both coatings were viable, providing ample redundancy. However, the Ni coating offered higher reflectivity, making it the preferred choice. At energies greater than 10 keV, the mirrors were moved out of the beam path. The beam height change between using and not using the mirrors was 1.16 mm, which could be accommodated by lifting the downstream support stage. The HRM box served as a support base and provided vacuum protection for the mirrors to enable the control of the incident angle and coating switching.

The effectiveness of the HRM in the XAFS experiments was validated through K-edge XAFS testing on a Ti foil, as shown in Fig. 5. The total absorption length of the Ti foil at

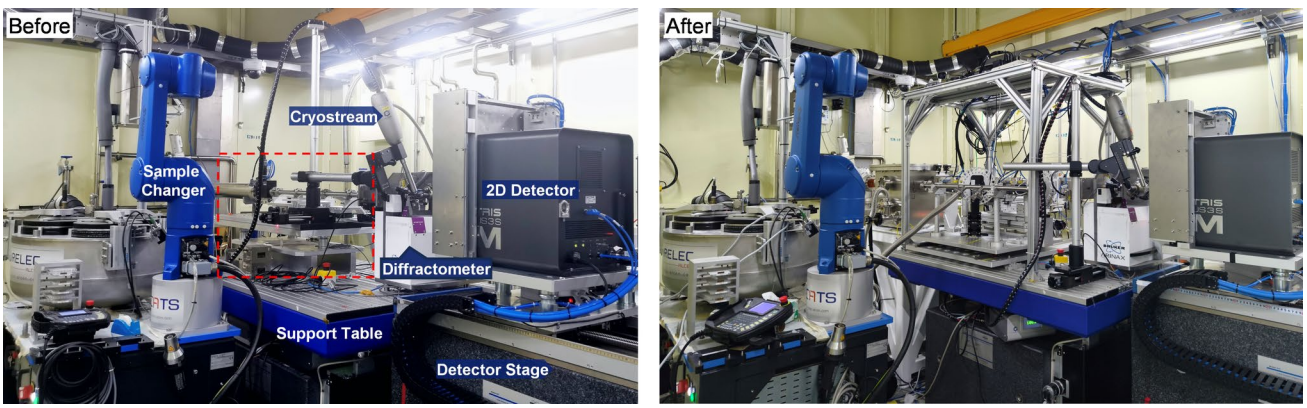

Fig. 2 (Color online) Experimental hutch before (left) and after (right) XAFS station incorporation. The red-boxed area indicates the XAFS station

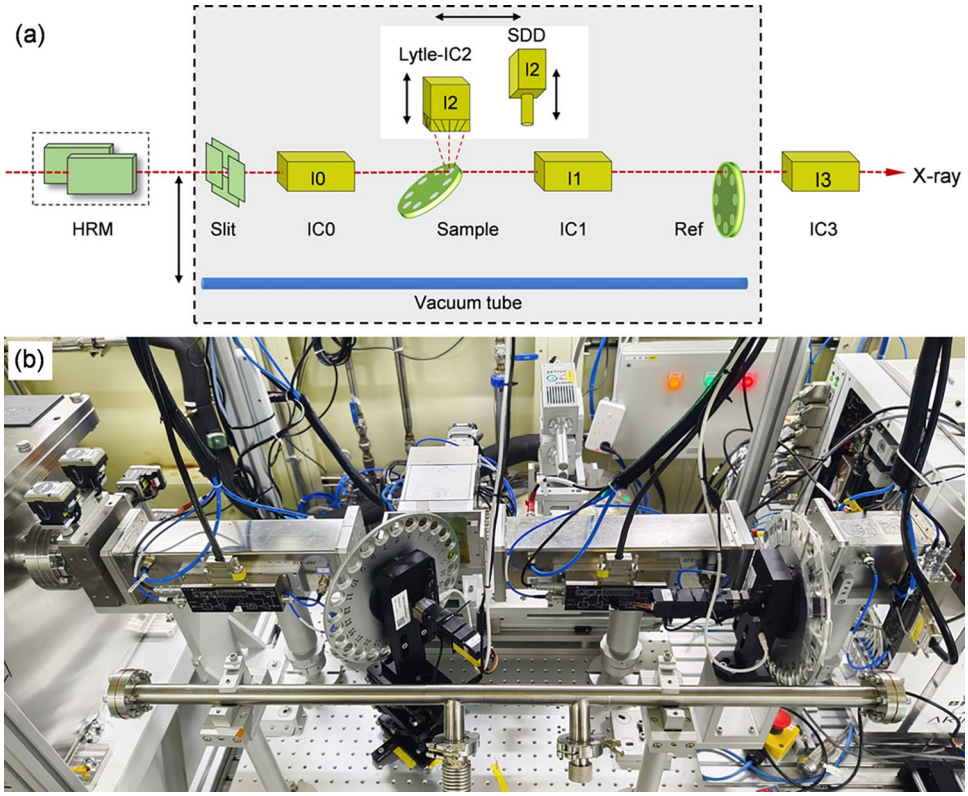

Fig. 3 (Color online) **a** Schematic and **b** physical layouts of the XAFS experimental station

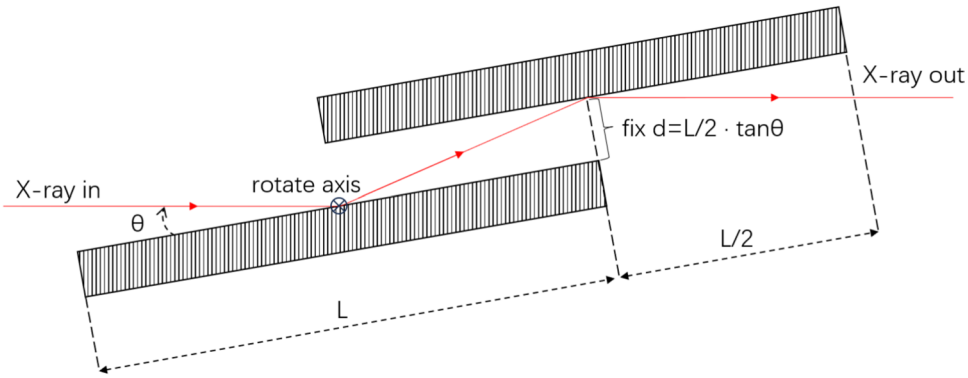

Fig. 4 Optical geometry of HRM

5 keV was 3.8. Given that the harmonic content was higher in lower-energy regions, an increased sample thickness exacerbated the amplitude attenuation effect. The spectral shape was severely distorted in the absence of HRM but returned to its normal state upon the inclusion of HRM. These results clearly demonstrate the effectiveness of HRM in suppressing harmonics and the necessity of acquiring reliable XAFS data.

3.2 Testing platform

As shown in Fig. 3, three ionization chambers were arranged along the X-ray path, with the sample wheel and reference sample wheel positioned between them. The I0 ionization chamber monitors the incident beam intensity, I1 records the beam intensity transmitted through the sample, and I3 records the beam intensity transmitted through the reference sample. Because synchrotron X-rays are linearly polarized in the horizontal plane of the synchrotron[34], the scattering interference is weakest in the direction perpendicular to the beam path within the horizontal polarization plane. Therefore, fluorescence detector I2 was placed along the perpendicular direction to collect the fluorescence of the sample. By simultaneously collecting the I0, I1, I2, and I3 signals, we obtained the following: a) the transmission-mode XAFS of the sample using Eq. (1), (b) the fluorescence-mode XAFS of the sample using Eq. (2), and (c) the transmission-mode XAFS of the reference sample using Eq. (3):

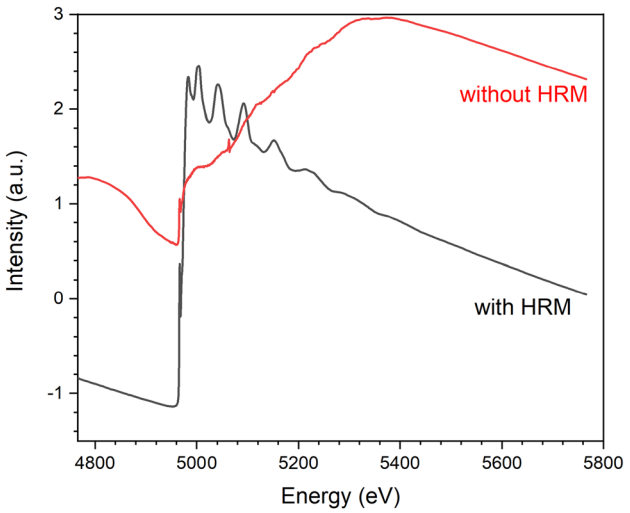

Fig. 5 (Color online) XAFS spectra of the Ti foil collected with (black) and without (red) HRM

$$\mu_{\text{Sample}}d = \ln(\text{I0}/\text{I1}) \tag{1}$$

$$\mu_{\text{Sample}}d \propto \text{I2}/\text{I0} \tag{2}$$

$$\mu_{\text{Reference}}d = \ln(\text{I1}/\text{I3}) \tag{3}$$

where μ represents the absorption coefficient, and d is the sample thickness along the beam path. The advantage of this setup lies in its ability to simultaneously acquire both transmission and fluorescence spectra from a sample to enhance experimental efficiency. Because a given sample is more suitable for either the transmission or fluorescence mode, the decision on which mode to use can be deferred to the post-processing stages. Moreover, by concurrently collecting reference sample data, an energy calibration standard was incorporated into the data of each sample to enable a comparison between datasets obtained under varying instrument conditions.

There are two types of fluorescence detectors: a Lytle ionization chamber and an SDD. The Lytle detector has the advantage of handling higher-count-rate signals, and it is simple to operate with low maintenance costs. The SDD detector distinguishes XRF signals from different elements, which is particularly useful for studying multi-element materials. The fluorescence detectors are mounted on a two-level electric stage for rapid switching, as shown in Fig. 6. Both detectors have an upper stage to adjust the distance between the detector and sample along the perpendicular direction. The detectors and their upper stages shared a common lower stage for movement parallel to the beam path. The motor positions for different detectors under operation or standby states were predefined,

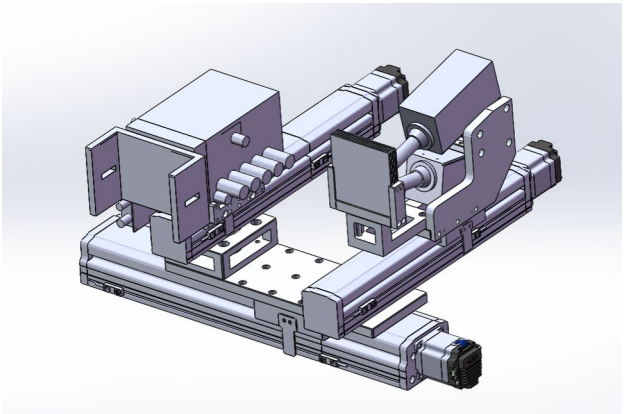

Fig. 6 (Color online) Electric switching stage for the Lytle ionization chamber and SDD fluorescence detectors

which allowed for one-click rapid switching between the fluorescence detectors.

3.3 Experiment mode

(i) *Transmission mode*: I0, I1, and I3 are fixed-length ISIC series standard gas ionization chambers from the Tianjin Jingshenfang company with effective lengths of 30 cm for I0 and I1 and 10 cm for I3. The He/N_2/Ar gas mixture ratios of each ionization chamber were predefined for every absorption edge to maintain absorption ratios of approximately 20% for I0, 80% for I1, and 100% for I3 and were executed through an automatic gas delivery system (as shown in Fig. 7). This ratio allows the transmission data of the sample to approach the optimal signal-to-noise ratio while preserving a sufficient number of transmitted photons for the reference sample to achieve good data quality. The transmission mode is applicable for samples with higher concentrations and generally requires an effective absorption concentration μ_A/μ_T greater than 10–20 μ%.

(ii) *Lytle fluorescence mode*: A Lytle ionization chamber [35] with 100% Ar working gas was employed. The Lytle chamber has no energy discrimination capability and cannot distinguish target fluorescence signals from other fluorescent and scattered photon backgrounds through energy identification. However, the Lytle detector employs a combination of a Z-1 filter and Soller slit [36–38] that effectively suppress background noise while preserving the target fluorescence to thereby enhance the signal-to-noise ratio. Because the fluorescent and scattered photons have different energies, the Z-1 filter can remove most of the scattered photons while preserving most of the fluorescence. The Soller slit, focused on the sample, blocks secondary photons produced by the filter while allowing the majority of the fluorescence of the sample to pass through. The Lytle detector offers a wide acceptance angle for fluorescence signals, reaching up to

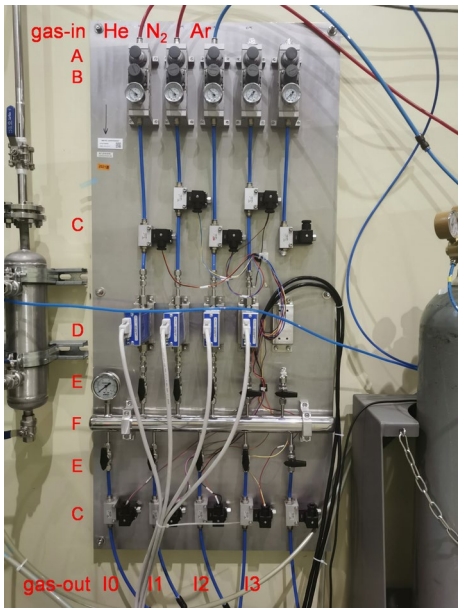

Fig. 7 (Color online) Automatic gas delivery system for ionization chambers. A: Isolation valve; B: press regulator; C solenoid valve; D: flow control valve connected to MKS964 control system; E: manual valve; F: gas-mixing chamber

10% × 4π, and has no saturation current limit, thus enabling the detection of high-intensity signals. Fluorescence-mode data are susceptible to self-absorption effects that can lead to XAFS amplitude attenuation. To mitigate the impact of self-absorption, this experiment mode is generally employed for either low-concentration thick samples, in which the effective absorption concentration is recommended below 10 μ% and the total absorption thickness μ_Td exceeds 3, or high-concentration thin samples, in which the edge jump $\Delta\mu_A d$ is less than 0.1.

(iii) *SDD fluorescence mode*: Fluorescence signals were collected using a 3-element Vortex-90EX [39] silicon drift detector (SDD) and processed using an Xspress 3 Mini (X3M) electronics readout system. This detector boasts energy discrimination capability and enables the selective extraction of the target fluorescence signal, which thereby enhances the signal-to-noise ratio. However, each probe has a saturation count rate of approximately 2 Mcps, which imposes an upper limit on the signal-to-noise ratio. To increase the proportion of the target fluorescence signals within the saturation count range, filters must be incorporated in front of the SDD to attenuate a significant number of scattered photons. This experimental mode primarily serves as a complement to the Lytle fluorescence mode and is typically applied when sample concentrations are lower than the detection limit of the Lytle method or when there is substantial background fluorescence interference. In such cases, the target signal is submerged in the background noise, which renders the Lytle detector ineffective, whereas the energy discrimination capability of the SDD is advantageous.

3.4 Sample loading condition

The reference sample wheel was equipped with a complete set of reference metal foils [40] from the Exafs Materials Company, allowing remote switching of the desired samples. There was ample space at the sample position to accommodate remote sample loading with the sample wheel as well as manual sample loading with an in situ sample holder or other sample holder. The sample wheel assumed that all samples are centered at each hole. That is, as long as one hole was aligned, the other holes were also aligned. Thus, the sample wheel was suitable for uniformly prepared large samples and thereby facilitated rapid sample exchange. The sample wheel had 26 holes, each with a diameter of 15 mm and spacing of 25 mm. The samples were attached to the center of the holes for loading. Because Hole #0 was used as a blank, the maximum sample capacity was 25. The wheel was attached to the base using magnets, enabling rapid wheel replacement. The position reset function of the sample wheel eliminated position errors caused by stress during wheel replacement. In particular, when a fixed pointer on the wheel passed the photoelectric sensor at the base, the current position was defined as zero. The sample wheel was generally placed at an angle of 45°relative to the beam path to accommodate the simultaneous collection of transmission and fluorescence data.

4 XAFS control system

The software control system for the XAFS experiments was developed using LabVIEW, which is a system design platform, and a development environment created by National Instruments (NI), which is also known as the Laboratory Virtual Instrument Engineering Workbench. The advantages of LabVIEW are its user-friendly graphical user interface and easy-to-control modules, which are adaptable to various types of hardware. The SDD electronics readout system, along with the motion control systems of existing beamline equipment, including monochromators, focusing mirrors, and support stands, were developed based on distributed experimental physics and industrial control systems (EPICS). The communication mode of LabVIEW facilitates seamless data sharing with the EPICS system. Newly incorporated devices, such as the HRM, fluorescence detector stage, automatic gas delivery system, sample wheel, ADC, and remote gain controller communicate via Ethernet and connect to the local network through switches, interacting with the XAFS software computer.

4.1 Experiment preparation

The XAFS software is distinguished by its highly integrated architecture. This software comprehensively manages the various equipment configurations that are involved in the XAFS experiments, which thereby enhances efficiency and convenience throughout the experimental process. At the start and end of each XAFS experimental run, the software enabled effortless switching between diffraction and XAFS modes. This software can (a) control the focusing mirror to adjust the focus position, (b) sequentially control the HRM coating and height of the support stage for an unobstructed optical path, (c) move the testing platform to switch between the vacuum tube and XAFS devices, and (d) manage the automatic gas filling system, thus filling the I3 ionization chamber with 100% N_2 during the diffraction mode to minimize light attenuation.

Before the formal XAFS data acquisition for each element to be measured, this software has designed the following preparation workflow: (1) mount the sample using a sample wheel or other sample holder and replace filters for fluorescence detectors; (2) change the gas for ionization chambers through the gas delivery system; (3) optimize the optical configuration, which involves adjusting the HRM working coating, controlling the support stage to compensate for beam height change after HRM, and optimizing the parallelism of the monochromator for maximum photon flux; (4) replace the reference sample via the reference sample wheel and collect its XANES data to calibrate the monochromator energy; and (5) select the appropriate fluorescence detector by controlling the two-level electric stage. Except for the first step, which requires on-site manual operation, all other steps integrate the basic subtasks into a one-touch control to accomplish the desired task. This highly integrated control system significantly reduces the need for onsite fine-tuning equipment, thus enabling remote experimentation.

4.2 Data acquisition

The hardware architecture involved in XAFS data collection is shown in Fig. 8. The monochromatized beam passed through the ionization chambers and samples, with attenuated photons and excited fluorescence detected and fed into the data acquisition system. The initial signal currents from the I0, I1, and I3 ionization chambers as well as the I2 Lytle detector were in the fA–uA range. Being cautious regarding the output voltage stability of the high-voltage supply for ionization chambers is crucial, as this could impact the background noise. We utilized the HV-3000 model from the Tianjin Jingshenfang Company with an output voltage ripple coefficient of less than 0.001%. Direct long-range transmission and the reading of initial signals are susceptible to transmission losses and electromagnetic interference, which introduce significant noise. To improve the signal-to-noise ratio of the subsequent electronics, current signals from each ionization chamber were connected to a current-to-voltage amplifier (Femto DLPCA-200), and the amplified voltage signals were then fed to a 4-channel ADC acquisition card (Geekootech FS3326S) and converted to digital signals. The ADC card has a 16-bit resolution and maximum sampling rate of 2 MS/s per channel. However, a 0.5 MS/s rate is used to avoid buffer overflow issues. A 4-channel remote gain controller was developed for the amplifier DLPCA-200 to enable the remote control of the gain for the four ion chambers. The initial current signal from the I2 SDD fluorescence detector was converted into a digital signal by a readout

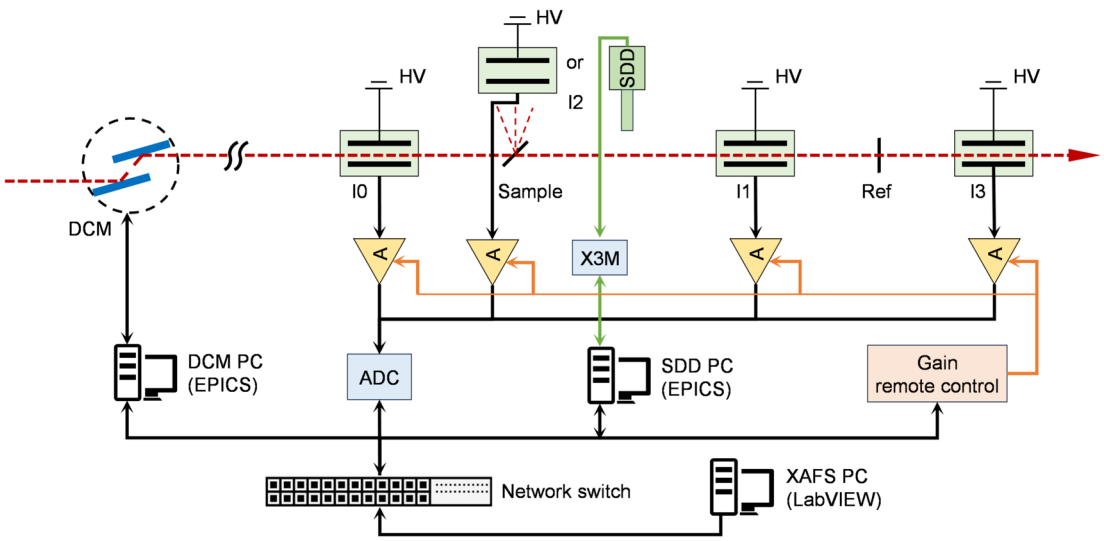

Fig. 8 (Color online) XAFS data acquisition hardware architecture

system (Quantum Detectors Xspress 3 Mini) and read using an acquisition program.

The XAFS data acquisition system employed a conventional step-by-step scan mode, as shown in Fig. 9. Here, the monochromator was driven to a specific energy and allowed to stabilize for a moment. Subsequently, the real-time energy readback was recorded. In this step, we did not repeatedly drive the monochromator to fine-tune its readback to the exact energy specification, as this could introduce worse energy errors owing to backlash. The strategy of driving the monochromator once and recording the energy readback value effectively improves the accuracy of energy measurements while conserving time. The ADC and SDD commenced data acquisition and transmitted the data to the XAFS computer. The acquisition software calculated and recorded the average count rate within the integration time, thereby completing the collection of that data point. This process was repeated for the next energy point (cycling) until the spectrum was fully acquired. Collecting a full XAFS spectrum typically required approximately 15 min (integration time of 1 s). Moreover, to prevent signal saturation, which can lead to data distortion, we introduced an innovative auto-gain control function prior to formal data collection. This function performed a preliminary scan of the entire spectrum, identified the maximum current value for each detector, and automatically adjusted the gain of the corresponding amplifier to ensure that the amplified voltage

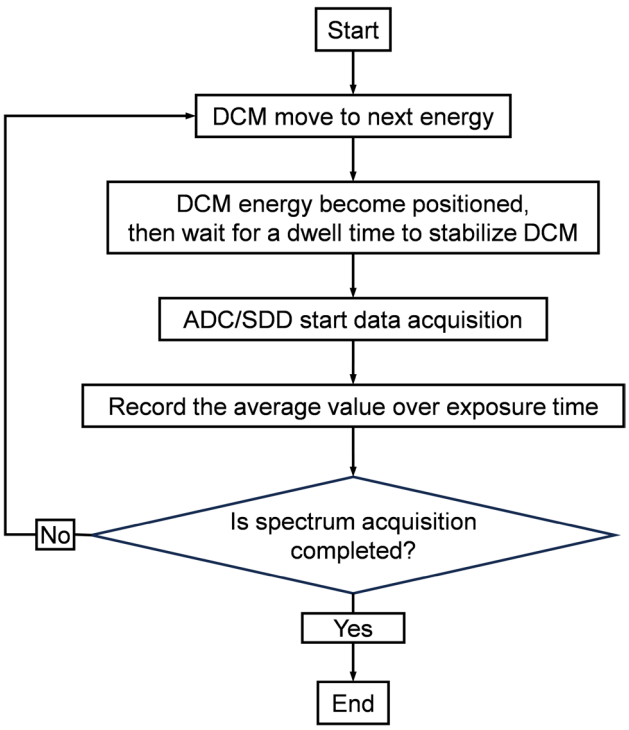

Fig. 9 (Color online) Flowchart for the XAFS data acquisition of a single spectrum

was as large as possible without saturation. This function can provide a linear response and an optimal signal-to-noise ratio across various signal intensities, which guarantees the accuracy and reliability of the data.

The highly integrated XAFS control system enables simple data acquisition and automated measurements based on the sample wheel. A sample evaluation feature was incorporated to enhance the efficiency of the automatic measurement. By collecting data before and after the absorption edge in both the blank (Hole #0) and sample-mounted states, parameters including the total absorption thickness, effective absorption concentration, transmission edge jump, and fluorescence edge jump-to-background ratio can be calculated. These parameters assist users in rapidly assessing whether data are worth collecting and optimizing sample preparation. The selected samples were subjected to automated sample exchange and data acquisition. Notably, automatic measurement is applicable only to samples with the same absorption edge using the Lytle detector because manual filter replacement is required for different elements. Moreover, samples that require SDD detection often involve more complex situations, which makes them more suitable for individual treatment.

4.3 Data format

The data adopted the XAFS Data Interchange (XDI) standard [41] format specified by the International X-ray Absorption Society (IXAS). The XDI format aims to share XAFS data across continents, decades, and analysis toolkits, and it is the only accepted data format for the X-ray Absorption Data Library (XASLIB, https://www.xaslib.xrayabsorption.org). As depicted in Fig. 10, our data consist of two parts: a metadata header and data table, separated by "#—". Our header includes details, such as the data source, absorbing element, sample evaluation, experimental setup, and user comments, which provide a comprehensive record of the experiment. The data columns correspond to the energy; raw data of I0, I1, I2, and I3; and converted absorption data of the transmission, fluorescence, and reference.

5 XAFS platform performance

To evaluate the performance of the XAFS experimental platform, we inspected various aspects of its capabilities. The common parameters are summarized in Table 1. The BL17B XAFS platform has an energy range of 5–23 keV, which permits XAFS data collection for elements spanning Ti to the K-edge of Ru and Cs to the L3-edge of Bi, as shown in Fig. 11. Notably, Tl, Pm, and actinide elements are not permitted for testing at this platform. This decision was based on concerns regarding chemical toxicity and experimental

Fig. 10 (Color online) XAFS data format for BL17B

```
# XDI/1.0
# Acknowledgment.template: We thank the staff at SSRF BL17B of the National Facility for Protein Science
in Shanghai (NFPS), Shanghai Advanced Research Institute, CAS, for providing technical support in X-ray
absorption fine Structure data collection and analysis.
# Scan.start_time: 2024-06-14 03:07:27
# Total time: 1448.31 s
# Sample.name: Mn3O4
# Reference_Sample.name: Mn foil
# Element.symbol: Mn
# Element.edge: K
# Scan.edge_energy: 6539.0 eV
# NoSample_evaluation.total_absorption_thickness: x*mu_T=-0.438507
# Sample_evaluation.total_absorption_thickness: x*mu_T=4.02
# Sample_evaluation.edge_step: x*mu_edge_step=2.45 (roughly evaluated)
# Sample_evaluation.effective_absorption_concentration: mu_A/mu_T=(x*mu_edge_step)/k/(x*mu_T)=69.68%%,
where jump ratio k=0.8750
# Sample_evaluation.result: Alarm,  Notice the Thickness /Self-absorption Effect
# Scan.Mono_waiting_time: 0.10 s
# Scan.mode: E  E  E  E  E  E  E
# Scan.region: -200  -15  30  150  250  400  600  1000
# Scan.step: 5  0.30  1  2  3  4  5
# Scan.time: 1  1  1  1  1  1  1
# Mono.name: Si 111
# Mono.d_spacing: 3.1356
# Beamline.collimation: 2.8mrad grazing-angle Rh-coated mirror
# Beamline.focusing: 2.8mrad grazing-angle Rh-coated mirror
# Beamline.harmonic_rejection: double 5.8mrad grazing-angle Ni-coated mirror
# Beamline.name: NFPS BL17B1
# Facility.name: SSRF
# Facility.energy: 3.50 GeV
# Facility.xray_source: SSRF bending magnet
# Detector.I0: --i0--     ion chamber 30cm 53%He 47%N2
# Detector.I1: --itrans-- ion chamber 30cm 90%N2 10%Ar
# Detector.I2: --ifluor-- Lytle 6.6cm Lytle 6.6cm 100%Ar  /SDD
# Detector.I3: --irefer-- ion chamber 10cm 100%Ar
# Column.1: energy eV
# Column.2: i0
# Column.3: itrans
# Column.4: ifluor
# Column.5: irefer
# Column.6: mutrans
# Column.7: mufluor
# Column.8: murefer
# ////////////////////////////////////////////////////////////////////
# User_comments: cas: 1317-35-7, Aladdin, M301684
#-------------------------------------------------------------------
# energy    i0    itrans    ifluor    irefer    mutrans    mufluor    murefer
6338.997  3.835925E+0  7.277620E-1  8.853982E-1  2.262383E-1  1.662192E+0  2.308174E-1  1.168385E+0
6344.003  3.848476E+0  7.361238E-1  8.892529E-1  2.309254E-1  1.654034E+0  2.310662E-1  1.159304E+0
6349.001  3.861939E+0  7.448589E-1  9.006759E-1  2.358834E-1  1.645730E+0  2.332186E-1  1.149857E+0
```

Table 1 BL17B XAFS platform parameters

Facility	SSRF
Light source	Bend Magnet
Electron energy (GeV)	3.5
Magnetic field intensity (T)	1.27
Beam intensity (mA)	200
Beamline acceptance angle ($mrad^2$)	1.5×0.1
Energy range (keV)	5–23, 7–21(recommended)
Energy resolution ($\Delta E/E$)	2×10^{-4} at 12 keV
Flux at sample (photons/s)	2.2×10^{11} at 12 keV
Focused spot size (mm^2)	1.5×0.6 ($H\times V$)
Harmonic rejection effect	XAFS amplitude attenuation < 1%

safety, despite the L-edge energies being within the accessible range of the monochromator. To measure the XAFS sample spot size, we used X-ray-sensitive exposure paper to record the central beam spot at the sample position. As depicted in Fig. 12, the spot size is approximately 1.5 mm × 0.6 mm ($H\times V$). By recording the current values of the 100% N_2-filled I0 ionization chamber under various incident beam energies, the corresponding beam flux was calculated using Hephaestus software [42]. As shown in Fig. 13, the flux in the central energy range (7–21 keV) is on the order of 10^{11} photons/s, which is our recommended working energy range. For 5–7 keV, the flux decreases quickly, owing to absorption by substances along the optical path. At 21–23 keV, the flux declines quickly with the reflectivity of the Rh-coated collimating and focusing mirrors. Nevertheless, the minimum flux within the XAFS energy range

Fig. 11 (Color online) Elements measured on a BL17B XAFS experimental platform

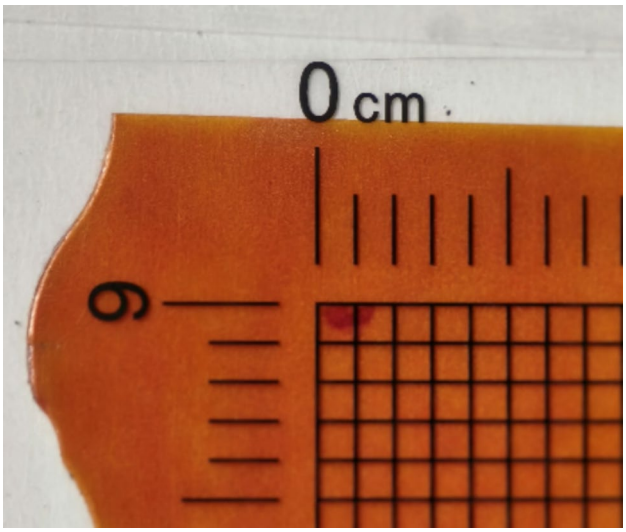

Fig. 12 (Color online) Beam spot on the XAFS sample recorded using X-ray exposure paper

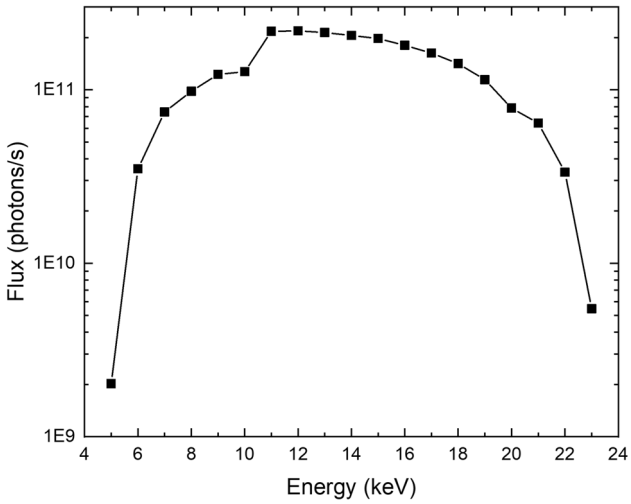

Fig. 13 Flux distribution at the XAFS sample position

was greater than 10^9 photons/s, which allowed high-quality data collection for high-concentration samples. As shown in Fig. 14, high-quality K-edge XAFS data were obtained at the experimental energy limits of Ti and Ru foils. The pre-edge peak of the Ti foil, which was approximately 2 eV wide, was clearly observed. The amplitude and signal-to-noise ratio of the EXAFS typically decrease rapidly with an increasing k value at a rate of k^{-2}. However, both EXAFS spectra in Fig. 14 remain smooth up to 15 $Å^{-1}$ without significant noise, demonstrating the capability of the platform to acquire high-quality data within its working energy range.

We further assessed the detection limits achievable under different experimental modes to provide guidance for selecting the optimal experimental mode for various sample conditions. We prepared copper (II) phthalocyanine (CuPc, $C_{32}H_{16}CuN_8$) samples diluted with LiF at varying Cu concentrations, collected their Cu K-edge XAFS spectra, and determined the detection limits based on the signal-to-noise ratios of the EXAFS and XANES data. As shown in Table 2, the mass fractions of the samples range from 3.4 wt% to 0.01 wt%, and their corresponding Cu absorption concentration (μ_A/μ_T) decreased from 60 to 0.3 μ%. To ensure the accuracy of the concentration, low-concentration samples were further diluted with high-concentration samples. Each sample was meticulously ground to ensure uniform mixing and then compressed into tablets with a diameter of 10 mm. Uniform tablet thickness helps avoid the pinhole effect [43], which can also lead to data distortion. The quantity of each sample is controlled to have a total absorption thickness

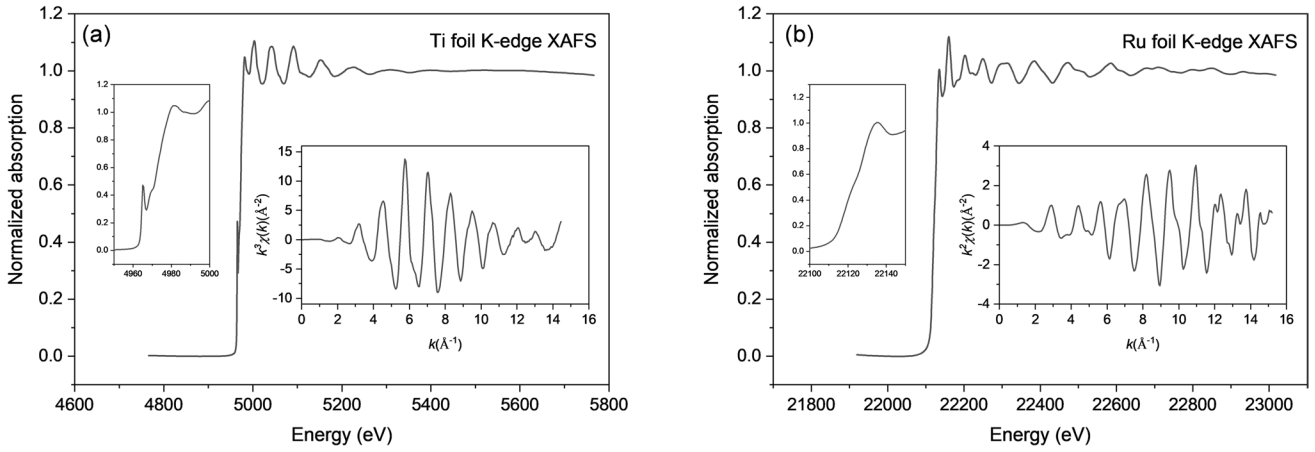

Fig. 14 K-edge absorption spectra of the **a** Ti and **b** Ru foils collected from BL17B

Table 2 Different Cu-concentration CuPc samples diluted with LiF

Sample	Mass fraction w_A/w_T	Absorption concentration μ_A/μ_T	Total absorption thickness $\mu_T d$	Jump edge $\Delta\mu_A d$
1	3.4%	60%	2.5	1.3
2	0.7%	20%	3.2	0.6
3	0.3%	10%	3.2	0.3
4	0.15%	5%	3.4	0.15
5	0.07%	2.5%	2.8	0.06
6	0.04%	1.5%	2.7	0.035
7	0.014%	0.5%	3.8	0.016
8	0.01%	0.3%	3.1	0.009

(μ_Td) of 2–4, which maximizes the signal-to-noise ratio according to the Nordfors criterion [44]. The actual measured total absorption thickness and jump edge in Table 2 aligned with the intended concentration, demonstrating the reliability of the sample preparation.

Normalized Cu K-edge EXAFS data for the diluted CuPc samples are shown in Fig. 15(a). The higher-concentration data exhibit better signal-to-noise ratios. In transmission mode, the 3.4 wt% sample remained smooth up to 14 Å^{-1}. When it drops to 0.3 wt%, the data signal-to-noise ratio decreases, but the data are reliable up to 12.5 Å^{-1}. Compared with the Lytle fluorescence data, the transmission data of this sample exhibited less noise but significant distortion beyond 12.5 Å^{-1}. Hence, 0.3 wt% (10 μ%) is the EXAFS detection limit for the transmission mode. Therefore, using the transmission mode is recommended for samples both with a concentration above 10% and a jump edge greater than 0.2. In the Lytle fluorescence mode, noise becomes more noticeable when the Cu mass fraction drops to 0.04 wt% (1.5 μ%). However, the data remain consistent with the real signal trend until 12.5 Å^{-1}, which is acceptable. In the SDD

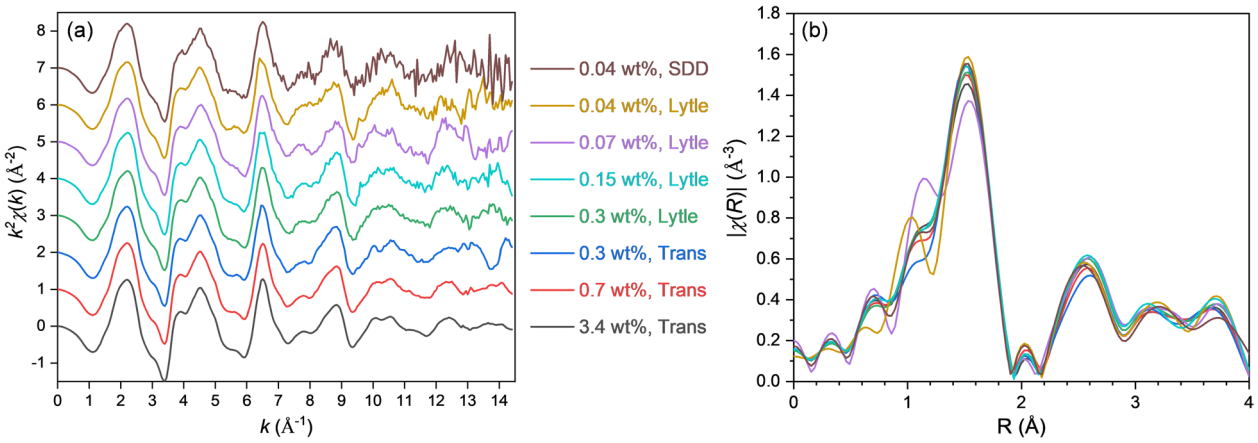

Fig. 15 (Color online) **a** k^2-weighted EXAFS spectra of LiF-diluted CuPc samples collected at BL17B and **b** the corresponding Fourier transforms

fluorescence mode, the EXAFS data of the 0.04 wt% sample show increased noise compared with the corresponding Lytle mode data, yet it aligns better with the actual signal. This is because the SDD selectively collects characteristic fluorescent signals; however, the total intensity is not as high as that of the Lytle detector. Therefore, 0.04 wt% (1.5 μ%) was proposed as the EXAFS detection limit for the fluorescence mode.

Figure 15(b) shows the Fourier transforms of the k^2-weighted Cu K-edge EXAFS spectra of CuPc samples with different Cu concentrations. The Fourier transform k-range is 3–12 Å^{-1}. All the data exhibit similar peak shapes within the range of 1.3–4 Å, especially at the first shell at 1.53 Å, owing to the nearest neighboring nitrogen atoms. The peak heights show a fluctuation of approximately 10%, which is reasonable because of the experimental error. These results indicate that the low-concentration data reflect real information and possess good reliability. Moreover, for samples collected under the Lytle mode (0.07 and 0.04 wt%), pseudo-peaks appear near 1.1 Å, which are caused by noise. These results suggest that data from low-concentration samples near the detection limit should be handled with caution. Fitting analyses were conducted on the first shell to quantitatively assess the reliability of the low-concentration data. The R fitting range is 1.3–2 Å for (0.07 wt%, Lytle) and (0.04 wt%, Lytle), and 1–2 Å for others. Table 3 shows the fitting results, indicating that the Cu–N interatomic distance d in the first shell for all samples is approximately 1.94 Å, with the coordination number N ranging from 3.8 to 4.1. Exceptions include (0.04 wt%, Lytle), which has a d value of 1.95 Å, and (0.07 wt%, Lytle), which has a slightly lower N value of 3.5. These results further validate/s the conclusion that low-concentration data can also be reliable; however, when handling low-concentration samples near the detection limit, being vigilant about false peaks and their potential impacts is essential.

The normalized Cu K-edge XANES data for the diluted CuPc samples are shown in Fig. 16. The detection limit for XANES was as low as 0.01 wt% (0.3 μ%), which was approximately one-fifth of that for EXAFS. For samples with concentrations exceeding this threshold, the noise in the XANES data was insignificant; however, potential issues with data distortion must not be overlooked. Such risks can be effectively mitigated by employing appropriate experimental modes. In transmission mode, the jump edge of the 0.15 wt% (5 μ%) sample is only 0.15. Moreover, lower concentrations, along with fewer jump edges, can introduce distortion. Hence 0.15 wt% (5%) can be regarded as the XANES detection limit for the transmission mode, with a recommended jump edge above 0.2. In the Lytle fluorescence mode, the self-absorption effect must be considered. The XANES data of the 0.15 wt% (5 μ%) sample align with that of the 3.4 wt% sample, indicating no significant self-absorption effect below this concentration. The Lytle mode is capable of detecting concentrations as low as 0.014 wt% (0.5 μ%), with XANES signals remaining consistent with actual signatures. The SDD fluorescence mode further enhanced the sensitivity, allowing detection down to 0.01 wt% (0.3 μ%).

In summary, the above experiments demonstrate that for EXAFS, the detection limit for the transmission mode is 0.3 wt% (10 μ%). Samples with concentrations above this value are recommended to be tested in the transmission mode and to maintain a jump height of 0.2 or higher. For concentrations below that, the fluorescence mode is more suitable with a detection limit as low as 0.04 wt% (1.5 μ%). In the case of XANES, the corresponding detection limits decrease further to 0.15 wt% (5 μ%) and 0.014 wt% (0.5 μ%). Notably, the detection limit mentioned here was derived under specific ideal conditions: The samples were primarily

Table 3 Structural parameters determined by EXAFS analysis of the first shell of CuPc samples with different Cu concentrations. Here, N and d represent the coordination number and interatomic distance, respectively. The amplitude reduction factor S_0^2 was fixed at 0.94. All the data share the same energy shift (ΔE) and Debye–Waller factor (σ^2) parameters, with ΔE fitted to 6.9 ± 0.8 and σ^2 fitted to 0.002 ± 0.001. The reliability factor R for this fit was 0.018

Sample	Shell	N	d (Å)
3.4 wt%, Trans	Cu–N	3.9 ± 0.3	1.94 ± 0.01
0.7 wt%, Trans	Cu–N	3.8 ± 0.3	1.94 ± 0.01
0.3 wt%, Trans	Cu–N	3.9 ± 0.4	1.94 ± 0.01
0.3 wt%, Lytle	Cu–N	4.0 ± 0.5	1.94 ± 0.01
0.15 wt%, Lytle	Cu–N	4.1 ± 0.8	1.94 ± 0.01
0.07 wt%, Lytle	Cu–N	3.5 ± 0.8	1.94 ± 0.02
0.04 wt%, Lytle	Cu–N	3.9 ± 0.9	1.95 ± 0.02
0.04 wt%, SDD	Cu–N	4.0 ± 2.5	1.94 ± 0.05

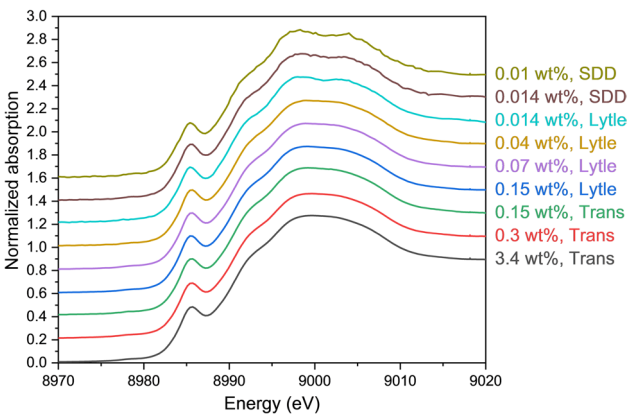

Fig. 16 (Color online) XANES data of the LiF-diluted CuPc samples collected at BL17B

composed of light elements without significant amounts of heavy atoms, which can generally introduce additional noise and increase the actual detection threshold. Although the detection limits may not be directly applicable to all complex samples, they still offer a valuable reference benchmark for assessing the feasibility of XAFS experiments. Again, these ultralow detection limits reaffirm the outstanding capability of the XAFS platform to acquire high-quality experimental data and render it particularly valuable for characterizing complex systems such as biological, environmental, and material samples that contain minute active components.

6 Conclusion

This work presents the successful development of an advanced XAFS platform at NFPS BL17B at SSRF, which complements the existing diffraction techniques and extends BL17B's structural characterization capabilities from long-range to short-range orders. The key innovations of this new platform are as follows. First, harmonic suppression mirrors were employed to effectively reduce higher-order harmonics in the beam to meet the stringent purity requirements of XAFS experiments. Second, the platform features a multifunctional testing station constructed with three transmission ionization chambers and two switchable fluorescence detectors to enable the simultaneous collection of transmission and fluorescence data as well as the synchronous comparison of target and reference samples, thereby enhancing data integrity and transferability. Furthermore, the platform incorporates a high-capacity automated sample wheel that enables remote sample loading and further integrates automatic evaluation and sampling functions to improve experimental efficiency. Automatic gain control ensures linearity and a high signal-to-noise ratio across various signal intensities to guarantee the accuracy and reliability of the data. The platform excelled within the energy range of 5–23 keV, covering the K-edges of elements from Ti to Ru and the L3-edges of elements from Cs to Bi. In an experiment conducted to study the Cu K-edge XAFS of low-concentration CuPc/LiF samples, we achieved an EXAFS detection limit as low as 0.04 wt% and an even lower XANES detection limit of 0.01 wt%. These results unequivocally demonstrate the exceptional performance of this platform in acquiring high-quality XAFS data, suggesting its valuable application in characterizing complex systems, including biological, environmental, and material samples that contain minute active components.

Author contributions All authors contributed to the study conception and design. Material preparation, data collection and analysis were performed by Lan-Lu Lu, Wen-Ming Qin, Luo-Zhen Jiang and Yang Liu. The first draft of the manuscript was written by Lan-Lu Lu and all authors commented on previous versions of the manuscript. All authors read and approved the final manuscript.

Data availability The data that support the findings of this study are openly available in Science Data Bank at https://cstr.cn/31253.11.scienceb.26799 and https://www.doi.org/https://doi.org/10.57760/sciencedb.26799.

Declarations

Conflict of interest The authors declare that they have no competing interests.

References

1. M.H. Jiang, X. Yang, H.J. Xu et al., Shanghai synchrotron radiation facility. Chin. Sci. Bull. **54**, 4171–4181 (2009). https://doi.org/10.1007/s11434-009-0689-y
2. W.Z. Zhang, J.C. Tang, S.S. Wang et al., The protein complex crystallography beamline (BL19U1) at the Shanghai synchrotron radiation facility. Nucl. Sci. Tech. **30**, 170 (2019). https://doi.org/10.1007/s41365-019-0683-2
3. Q.J. Xiao, T.T. Wu, K.W. Bao et al., Upgrade of crystallography beamline BL19U1 at the Shanghai synchrotron radiation facility. J. Appl. Crystallogr. **57**, 630–637 (2024). https://doi.org/10.1107/S1600576724002188
4. Q.S. Wang, K.H. Zhang, Y. Cui et al., Upgrade of macromolecular crystallography beamline BL17U1 at SSRF. Nucl. Sci. Tech. **29**, 68 (2018). https://doi.org/10.1007/s41365-018-0398-9
5. C. Giacovazzo, H.L. Monaco, G. Artioli et al., *Fundamentals of crystallography* (Oxford University Press, New York, 2011)
6. K. Li, L. Li, Y.C. Xu, Crystal structure determination of a chimeric FabF by XRD. Nucl. Sci. Tech. **28**, 123 (2017). https://doi.org/10.1007/s41365-017-0281-0
7. V.K. Pecharsky, P.Y. Zavalij, *The Powder diffraction pattern*, 2nd edn. (Springer, Boston, 2009)
8. J.A. Steele, E. Solano, D. Hardy et al., How to GIWAXS: grazing incidence wide angle X-ray scattering applied to metal halide perovskite thin films. Adv. Energy Mater. **13**, 2300760 (2023). https://doi.org/10.1002/aenm.202300760
9. Z.J. Zhu, L.L. Lu, C.Y. Li et al., GIWAXS experimental methods at the NFPS-BL17B beamline at Shanghai synchrotron radiation facility. J. Synchrotron Radiat. **31**, 968–978 (2024). https://doi.org/10.1107/S1600577524004764
10. M. Luo, S.J. Deng, L. Li et al., XAFS and SRGI-XRD studies of the local structure of tellurium corrosion of Ni–18%Cr alloy. Nucl. Sci. Tech. **30**, 153 (2019). https://doi.org/10.1007/s41365-019-0673-4
11. X.Y. Wang, H.B. Xie, Q. Guo et al., Molecular basis for METTL9-mediated N1-histidine methylation. Cell Discov. **9**, 38 (2023). https://doi.org/10.1038/s41421-023-00548-w
12. W.Y. Hu, B.X. Yang, Q.J. Xiao et al., Characterization of a promiscuous DNA sulfur binding domain and application in site-directed RNA base editing. Nucleic Acids Res. **51**, 10782–10794 (2023). https://doi.org/10.1093/nar/gkad743
13. Y.L. Cao, A. Yisimayi, Y.L. Bai et al., Humoral immune response to circulating SARS-CoV-2 variants elicited by inactivated and RBD-subunit vaccines. Cell Res. **31**, 732–741 (2021). https://doi.org/10.1038/s41422-021-00514-9
14. X.L. Cai, P.F. Wang, Z.J. Li et al., Mobilization and transformation of arsenic from ternary complex OM-Fe(III)-As(V) in the presence of As(V)-reducing bacteria. J. Hazard. Mater. **381**, 120975 (2020). https://doi.org/10.1016/j.jhazmat.2019.120975

15. J.L. Xu, L.K. Koopal, L.C. Fang et al., Proton and copper binding to humic acids analyzed by XAFS spectroscopy and isothermal titration calorimetry. Environ. Sci. Technol. **52**, 4099–4107 (2018). https://doi.org/10.1021/acs.est.7b06281
16. L.M. Kong, Y.Q. Sun, B. Zhao et al., Fabrication of red-emitting perovskite LEDs by stabilizing their octahedral structure. Nature **631**, 73–79 (2024). https://doi.org/10.1038/s41586-024-07531-9
17. P.D. Zhu, D. Wang, Y. Zhang et al., Aqueous synthesis of perovskite precursors for highly efficient perovskite solar cells. Science **383**, 524–531 (2024). https://doi.org/10.1126/science.adj7081
18. Y.M. Liang, S.S. Wang, M. Tang et al., Cascade synthesis of benzotriazulene with three embedded azulene units and large stokes shifts. Angew. Chem. Int. Ed. **62**, e202218839 (2023). https://doi.org/10.1002/anie.202218839
19. T.Q. Ma, E.A. Kapustin, S.X. Yin et al., Single-crystal X-ray diffraction structures of covalent organic frameworks. Science **361**, 48–52 (2018). https://doi.org/10.1126/science.aat7679
20. L. Jiang, X.X. Ye, D.J. Wang et al., Synchrotron radiation-based materials characterization techniques shed light on molten salt reactor alloys. Nucl. Sci. Tech. **31**, 6 (2019). https://doi.org/10.1007/s41365-019-0719-7
21. R. Sarangi, A biological perspective towards a standard for information exchange and reporting in XAS. J. Synchrotron Radiat. **25**, 944–952 (2018). https://doi.org/10.1107/s1600577518008779
22. M.C. Feiters, W. Meyer-Klaucke, X-ray absorption and emission spectroscopy in biology, in *Practical Approaches to Biological Inorganic Chemistry*. ed. by R.R. Crichton, R.O. Louro (Elsevier, Netherlands, 2020), pp.229–273
23. X.-W. Zhang, X.-J. Yan, Z.-R. Zhou et al., Arsenic trioxide controls the fate of the PML-RARα oncoprotein by directly binding PML. Science **328**, 240–243 (2010). https://doi.org/10.1126/science.1183424
24. C.C. Qu, P. Cai, K.X. Shi et al., Methods and mechanisms of the interactions between biomacromolecules and heavy metals. Chin. Sci. Bull. **67**, 4192–4205 (2022). https://doi.org/10.1360/tb-2022-0636
25. S. Yang, L.L. Lu, J. Li et al., Boosting hydrogen peroxide production *via* establishment and reconstruction of single-metal sites in covalent organic frameworks. SusMat **3**, 379–389 (2023). https://doi.org/10.1002/sus2.125
26. K. Sun, Y. Huang, Q.Y. Wang et al., Manipulating the spin state of co sites in metal-organic frameworks for boosting CO_2 photoreduction. J. Am. Chem. Soc. **146**, 3241–3249 (2024). https://doi.org/10.1021/jacs.3c11446
27. Z.J. Huang, Y. Bai, X.D. Huang et al., Anion–π interactions suppress phase impurities in FAPbI3 solar cells. Nature **623**, 531–537 (2023). https://doi.org/10.1038/s41586-023-06637-w
28. G. Bunker, *Introduction to XAFS: A Practical Guide to X-ray Absorption Fine Structure Spectroscopy* (Cambridge University Press, Cambridge, 2010)
29. Y. Iwasawa, K. Asakura, M. Tada, *XAFS Techniques for Catalysts, Nanomaterials, and Surfaces* (Springer, Switzerland, 2017)
30. H. Abe, XAFS spectral distortions related to optics issues, in *International Tables for Crystallography*. ed. by C.T. Chantler, F. Boscherini, B. Bunker (Wiley, US, 2024), pp.594–599
31. C. Glover, J. McKinlay, M. Clift et al., Status of the X-ray absorption spectroscopy (XAS) beamline at the Australian synchrotron. X-ray absorption fine structure–XAFS13: 13th international conference Stanford, California, USA. AIP, 2007, https://doi.org/10.1063/1.2644692
32. S. Calvin, *XAFS for Everyone* (CRC Press, Boca Raton, 2013), p.460
33. P. Sainctavit, J. Petiau, A. Manceau et al., Two-mirror device for harmonic rejection. Rev. Sci. Instrum. **60**, 2027–2029 (1989). https://doi.org/10.1063/1.1140867
34. J. Als-Nielsen, D. McMorrow, Sources, in *Elements of Modern X-ray Physics*. (Wiley, UK, 2011), pp.29–67
35. F.W. Lytle, R.B. Greegor, D.R. Sandstrom et al., Measurement of soft X-ray absorption spectra with a fluorescent ion chamber detector. Nucl. Instrum. Meth. Phys. Res. Sect A: Accel. Spectrometers Detect. Assoc. Equip. **226**, 542–548 (1984). https://doi.org/10.1016/0168-9002(84)90077-9
36. B. Bewer, Soller slit design and characteristics. J. Synchrotron Radiat. **19**, 185–190 (2012). https://doi.org/10.1107/S0909049511052319
37. E.A. Stern, S.M. Heald, X-ray filter assembly for fluorescence measurements of X-ray absorption fine structure. Rev. Sci. Instrum. **50**, 1579–1582 (1979). https://doi.org/10.1063/1.1135763
38. Y.Y. Yang, Q. Gao, S.Q. Gu et al., Soller slits automatic focusing method for multi-element fluorescence detector. Nucl. Sci. Tech. **27**, 115 (2016). https://doi.org/10.1007/s41365-016-0105-7
39. L.Y. Feng, J.S. Iwanczyk, B.E. Patt et al., Vortex: a new high performance silicon multicathode detector for XRD and XRF applications. Proc. SPIE **5198**, 103–110 (2004). https://doi.org/10.1117/12.511849
40. J. Wong, B. Rupp, in *Reference X-Ray Spectra of Metal Foils*. EXAFS Materials, Inc.: 871 El Cerro Blvd, Danville, CA, USA (1999).
41. B. Ravel, M. Newville, XAFS Data Interchange: a single spectrum XAFS data file format. J. Phys. Conf. Ser. **712**, 012148 (2016). https://doi.org/10.1088/1742-6596/712/1/012148
42. B. Ravel, M. Newville, ATHENA, ARTEMIS, HEPHAESTUS: data analysis for X-ray absorption spectroscopy using IFEFFIT. J. Synchrotron Radiat. **12**, 537–541 (2005). https://doi.org/10.1107/s0909049505012719
43. K.Q. Lu, E.A. Stern, Size effect of powdered sample on EXAFS amplitude. Nucl. Instrum. Meth. Phys. Res. **212**, 475–478 (1983). https://doi.org/10.1016/0167-5087(83)90730-5
44. B. Nordfors, The statistical error in x-ray absorption measurements. Arkiv Fysik **18**, 37–47 (1960)